metals

MDPI

Article

Effect of Volumetric Energy Density on the Evolution of the Microstructure and the Degradation Behavior of 3D-Printed Fe-Mn-C Alloys from Water-Atomized Powders

Quang Nguyen Cao [1], Abdelhakim Cherqaoui [1], Carlos Henrique Michelin Beraldo [1], Carlo Paternoster [1], Simon Gélinas [2], Carl Blais [2], Paolo Mengucci [3] and Diego Mantovani [1,*]

[1] Laboratory for Biomaterials and Bioengineering, CRC-I, Department of Min-Met-Materials Eng., University Hospital Research Center, Regenerative Medicine, Laval University, Québec, QC G1V 0A6, Canada; nguyen.cao-quang.1@ulaval.ca (Q.N.C.); abdelhakim.cherqaoui.1@ulaval.ca (A.C.); carlos-henrique.michelin-beraldo.1@ulaval.ca (C.H.M.B.); carlo.paternoster.1@ulaval.ca (C.P.)

[2] Laboratory for Powder Metallurgy, Department of Min-Met-Materials Engineering, Laval University, Québec, QC G1V 0A6, Canada; simon.gelinas.1@ulaval.ca (S.G.); carl.blais@gmn.ulaval.ca (C.B.)

[3] Department SIMAU & UdR INSTM, Università Politecnica Delle Marche, Via Brecce Bianche 12, 60131 Ancona, Italy; p.mengucci@staff.univpm.it

* Correspondence: diego.mantovani@gmn.ulaval.ca

Abstract: Additive manufacturing of metals opens new doors for innovation in custom-based productions in a wide range of fields, including medicine, even if it introduces new challenges that need to be addressed to guarantee the properties are equal to or superior to those of conventional fabrication processes. In this research, porous, biodegradable Fe-Mn-C alloys were fabricated using a 3D printing technique with four different printing energy densities ranging from 62.5 to 125.0 J/mm^3. The effect of printing energy density on the microstructure and degradation behavior was investigated. Lower energy densities resulted in higher pore density and the presence of unmelted powder particles, while the alloy printed at 104.2 J/mm^3 exhibited the lowest pore density and the smallest grain size. Degradation tests revealed that the highest pore density in the sample printed at 62.5 J/mm^3, and the lowest grain size in the sample printed at 104.2 J/mm^3 contributed to faster degradation rates. The alloy printed at the highest energy density, 125.0 J/mm^3, demonstrated the largest grain size and the slowest degradation rate. Energy-dispersive spectroscopy and Fourier transform infrared spectroscopy analyses identified manganese carbonate as the primary degradation product, with calcium phosphate forming as a secondary product. These findings provide a significant understanding of the relationship between printing parameters, microstructure, and degradation behavior, which are essential for optimizing the performance of Fe-Mn-C alloys in biodegradable material applications.

Keywords: 3D printing; Fe-based alloys; porosity; degradation; biodegradable metals

check for updates

Academic Editors: Irene Buj Corral and Felip Fenollosa-Artés

Received: 20 November 2024
Revised: 13 January 2025
Accepted: 20 January 2025
Published: 22 January 2025

Citation: Cao, Q.N.; Cherqaoui, A.; Henrique Michelin Beraldo, C.; Paternoster, C.; Gélinas, S.; Blais, C.; Mengucci, P.; Mantovani, D. Effect of Volumetric Energy Density on the Evolution of the Microstructure and the Degradation Behavior of 3D-Printed Fe-Mn-C Alloys from Water-Atomized Powders. *Metals* **2025**, *15*, 101. https://doi.org/10.3390/met15020101

Copyright: © 2025 by the authors. Licensee MDPI, Basel, Switzerland. This article is an open access article distributed under the terms and conditions of the Creative Commons Attribution (CC BY) license (https://creativecommons.org/licenses/by/4.0/).

1. Introduction

Additive manufacturing (AM), commonly referred to as 3D printing, has revolutionized the production of complex, customized components across a wide range of industries [1]. Among the materials used in AM, iron-based (Fe) alloys have gained significant attention due to their superior properties and potential for diverse applications [2,3]. In particular, Fe-based alloys are widely employed in both structural and biomedical applications because of their high strength, biodegradability, and biocompatibility [4].

In the biomedical field, Fe-based alloys are particularly promising for developing biodegradable implants, such as stents and bone scaffolds [5]. Their ability to degrade in physiological environments eliminates the need for removal surgeries after healing, making them particularly attractive for temporary implants [6]. However, achieving an optimal balance between strength, degradation rate, and biocompatibility requires careful control over the alloy's microstructure [5,6]. Alloying elements, such as manganese (Mn) and carbon (C), have proven effective in enhancing the mechanical properties and degradation rates of Fe alloys, making Fe-Mn-C alloys a promising material for biodegradable implant applications [7,8].

Manganese, as an austenite stabilizer, promotes the formation of austenitic phases in Fe-based alloys, enhancing ductility and toughness [7–10]. Carbon, when present in the matrix or as carbides, influences both the mechanical properties and degradation behavior of the alloy [8–10]. Moreover, Mn and C are known to exhibit moderate biodegradability and biocompatibility, further supporting their use in biomedical alloys [11]. For example, E. Mouzou et al. [12] and S. Gambaro et al. [7] developed Fe-Mn-C alloys with impressive mechanical properties, achieving ultimate tensile strengths of up to 1230 MPa and elongation beyond 50%. Immersion tests in modified Hanks' solution revealed accelerated initial degradation rates compared to pure Fe, though the formation of carbonates or phosphates avoids full degradation. Similarly, M.C. Conti et al. [9] increased the tensile strength of Fe-13Mn-1.2C to 1300 MPa via cold rolling, while immersion tests in Hank's solution (with or without albumin) showed that $MnCO_3$ and $FeCO_3$ formed a stable protective layer, reducing the degradation rate to 0.006 mm/year. These studies suggest that Mn and C are effective alloying elements for creating Fe-Mn-C alloys for biodegradable applications. However, traditional fabrication methods like casting, which produce dense structures, limit the biodegradability of these alloys [13–15].

To address this limitation, porous Fe-Mn-C alloys produced by 3D printing were selected for this work. In bone-contact applications, the evolution of microstructure is particularly critical for porous Fe-Mn-C alloys, which are often designed with specific porosity levels like bone structures in biomedical applications [16,17]. Control over the porosity and microstructure through precise regulation of energy density can influence both the mechanical integrity and degradation behavior in bone-contact physiologically relevant environments. This is especially important in porous Fe-Mn-C alloys, where controlled degradation rates are essential for biodegradable implants [9,10]. AM has demonstrated its capability to fabricate metallic materials with varying pore densities and geometries, allowing the degradation rate to be controlled [18–20].

One key factor affecting the properties of 3D-printed alloys is the energy density used during the AM process [21–23]. Energy density, which is a function of laser power, scanning speed, and layer thickness, significantly influences melting, solidification, and cooling rates during fabrication [24,25]. It plays a crucial role in determining the alloy's microstructure by affecting grain size, phase formation, porosity, and residual stresses. For instance, higher energy densities can lead to enhanced grain refinement and improved mechanical strength, but they may also introduce undesirable phases or excessive porosity that compromise the alloy's performance [26–28].

In this study, we systematically investigate the effect of energy density on the microstructure and degradation behavior of 3D-printed porous Fe-Mn-C alloys. By exploring how varying energy inputs impact porosity, grain size, phase composition, and corrosion properties, this work aims to provide valuable findings into optimizing Fe-Mn-C alloys for biodegradable implant applications.

2. Materials and Methods

2.1. Powder Preparation

Fe-Mn-C powder was prepared by water atomization from three initial bulk materials: 4 kg of Fe-Mn alloy, 16 kg of Fe-C AISI 1018 steel, and 151 g of carbon. The chemical composition of the initial bulk materials was listed in Table 1. After atomization, powder size in the range of 20–53 μm was used for printing. The atomized powder then underwent the reduction process to reduce the overall oxygen content. The reduction process was carried out in a tubular furnace (GSL1700X, Richmond, CA, USA) at 900 °C for 30 min under an atmosphere composed of 90 vol.% Ar and 10 vol.% H_2.

Table 1. The chemical composition of the initial bulk materials.

Materials	Chemical Elements (wt.%)			
	Fe	**Mn**	**C**	**Si**
Fe-Mn	13.61	85.72	0.16	0.51
AISI 1018	99.11	0.74	0.15	-
Graphite	-	-	99.99	-
Fe powder	99.99	-	-	-

2.2. Sample Preparation

The reduced powder described above was used for 3D printing by selective laser melting. The printing process was carried out by the EOS M100 3D printer (EOS GmbH, Krailling, Deutschland) in an argon atmosphere. Four printing conditions were defined to investigate the effect of printing energy density. Scanning speed was kept the same as 0.8 m/s. Laser power varied from 30 to 60 W. The printing energy density is calculated based on the following equation:

$$\mathrm{E} = \frac{P}{V.H.L},$$

where E is printing energy density, P is laser power, V is scanning speed, H is hatch distance, and L is layer thickness.

The detailed conditions are described in Table 2.

Table 2. Laser power and scanning speed of the printed sample.

Sample Name	Energy Density (J/mm^3)	Scanning Speed (mm/s)	Laser Power (W)	Hatch Distance (mm)	Layer Thickness (mm)
E1	62.5	800	30	0.03	0.02
E2	83.3	800	40	0.03	0.02
E3	104.2	800	50	0.03	0.02
E4	125.0	800	60	0.03	0.02

Samples were printed with the size of 10 mm × 10 mm × 2 mm. The printed samples were used for chemical analysis, structural analysis, and static degradation immersion tests.

The printed samples were then polished with SiC abrasive papers up to 800 grit. Successively, fine polishing was performed with diamond paste of 6 μm, 3 μm, and 1 μm, followed by ethanol rinsing and air drying for further investigations.

2.3. Degradation Behavior

The static immersion degradation tests were performed on as-printed samples with dimensions of 10 mm × 10 mm × 1 mm, in accordance with ASTM G31-03 standard guidelines for corrosion testing [29]. Prior to immersion, each specimen was precisely weighed using a high-accuracy digital balance (5-digit precision, Analytical Plus, Ohaus, Parsippany, NJ, USA). Three samples from each printing condition were prepared and immersed in Modified Hanks' Salt Solution (MHSS). The composition of MHSS was described in Table 3. The samples were suspended in a covered beaker containing 90 mL of MHSS, using nylon threads to ensure all the surface area of the samples was exposed to the solution. The tests were carried out in an incubator set to maintain a constant temperature of 37.0 ± 1 °C, with controlled conditions of 5 vol.% CO_2 and 90% humidity to simulate in vivo degradation environments.

Table 3. Salt concentration of the modified Hanks' salt solution (MHSS).

Solution Composition				
Deionized Water	**Salts**	**HEPES Acid**	**HEPES Na Salt**	**$NaHCO_3$**
1.4 L	9.7 g of Hanks' balanced salts	14.16 g	16.65 g	3.3 g

After a 14-day immersion period, the samples were carefully removed from the solution and subjected to ultrasonic cleaning in a 70% ethanol solution for 5 min to remove degradation products from the surface. Once cleaned, the specimens were re-weighed to assess mass loss and calculate the degradation rate. Following this, a comprehensive surface analysis of the degraded samples was conducted using Scanning Electron Microscopy (SEM) (Quanta 250, FEI Company Inc. Thermo-Fisher Scientific, Hillsboro, OR, USA) to observe morphological changes and Energy Dispersive X-ray Spectroscopy (EDS) to determine the elemental composition.

The medium after the static degradation tests was carefully processed to recover the degradation products. First, the waste solution, comprehensive of the degradation products, was centrifuged at 3000 rpm for 10 min, effectively separating the supernatant from the suspended degradation product. Once the supernatant was removed, the collected sediment was then soaked with a solution consisting of 50 vol.% pure ethanol and 50 vol.% deionized water to remove any soluble residual salt from the medium. The suspension was subjected to vortexing to ensure a thorough precipitate washing, followed by an additional centrifugation step to further concentrate the solid degradation products.

Once isolated, the solid particles were carefully dried at 37 °C under reduced pressure (30 Torr) to ensure complete desiccation without altering the chemical structure of the products. The dried degradation products were then subjected to detailed analysis using Scanning Electron Microscopy (SEM) to observe morphology of the particles, Energy Dispersive X-ray Spectroscopy (EDS) to determine the existing elements, and Fourier Transform Infrared Spectroscopy (FTIR) to identify the composition of the degradation products.

The degradation rate (DR) of the printed alloys was determined using the equation outlined in Equation (1), as prescribed by the ASTM G31-03 standard [29],

$$\mathrm{DR} = 8.76 \cdot 10^4 \, \frac{W}{A \cdot t \cdot \rho}. \quad (1)$$

In this equation, DR represents the degradation rate (mm/year), W is the mass loss (g), which is calculated as the difference between the sample's initial and final weight after the immersion test, A refers to the surface area of the sample (cm^2), t denotes the immersion time (h), and ρ corresponds to the material's density (g/cm^3). The degradation rates (DR) of the samples after static immersion tests in MHSS were expressed as mean values ± standard deviation.

2.4. Chemical Analysis

The composition of the starting bulk materials, the reduced powder, and the final printed samples was thoroughly characterized. The chemical composition of the metallic elements was determined using microwave plasma atomic emission spectroscopy (MP-AES), performed with an Agilent Technologies 4100+ MP-AES system (upgraded to a 4200-torch system) (Agilent, Santa Clara, CA, USA). This method allowed for precise quantification of key metallic elements present in the samples. In addition to the metallic analysis, the content of oxygen (O), carbon (C), and sulfur (S) was measured using specialized techniques. Oxygen and nitrogen levels were assessed through inert gas fusion analysis, conducted with a LECO ONH836 analyzer (LECO, St. Joseph, MI, USA), while carbon and sulfur concentrations were determined via combustion analysis using the LECO CS200 instrument (LECO, St. Joseph, MI, USA).

2.5. Structural Characterization

The microstructural characterization of the atomized powder, reduced powder, 3D-printed samples, degraded samples, and the corresponding degradation products was performed using a scanning electron microscope (Quanta 250, FEI Company Inc. ThermoFisher Scientific, Hillsboro, OR, USA). This SEM was equipped with an EDAX-Ametec energy-dispersive spectroscopy (EDS) system, enabling detailed microanalysis of the elemental composition. To investigate the crystallographic structure of the printed samples, X-ray diffraction (XRD) was employed using a Bruker D8 Advance diffractometer (Bruker, Billerica, MA, USA). This diffractometer utilized Cu-Kα radiation at an operating voltage of 40 kV and a current of 40 mA, covering the angular range of 2θ = 20–80°.

The XRD pattern analysis was conducted using the DIFFRAC.EVA software suite (2018 V4.3.0.1 (32 bit)), which facilitated the identification of crystallographic phases. Peak indexing was accomplished with the search/match feature, referencing the PDF 2 database from the International Center for Diffraction Data (ICDD). To further refine the analysis, the shape of the XRD peaks was analyzed using the OriginPro 2023 software package (Origin (Pro), Version 2023, OriginLab Corporation, Northampton, MA, USA).

2.6. Degradation Product Characterization

The degradation products formed after static immersion degradation tests were analyzed using attenuated total reflectance Fourier transform infrared spectroscopy (ATR-FTIR). This technique was implemented on an Agilent Cary 660 FTIR spectrometer (Agilent Technologies, MN, USA), which was equipped with a highly sensitive deuterated L-alanine doped triglycine sulfate (DLa-TGS) detector and a germanium-coated potassium bromide (Ge-KBr) beam splitter. The ATR-FTIR spectra were recorded over a broad wavelength range of 4000 to 400 cm^{-1}, with a spectral resolution of 4 cm^{-1}, ensuring accurate detection and characterization of the chemical bonds present in the degradation products.

3. Results

3.1. Powder Properties

Figure 1 shows the morphology of the atomized powder before and after reduction. In general, the powder size is in the range of 20–50 µm. Before reduction, the powder particles exhibit rough and porous surfaces, with the presence of potential oxide layers. These oxide layers and surface contamination can significantly affect the printing quality by interfering with particle fusion during the laser melting process. Therefore, the reduction process was conducted. After reduction, the particle surfaces appear significantly smoother, indicating that the reduction process effectively removed oxides and impurities.

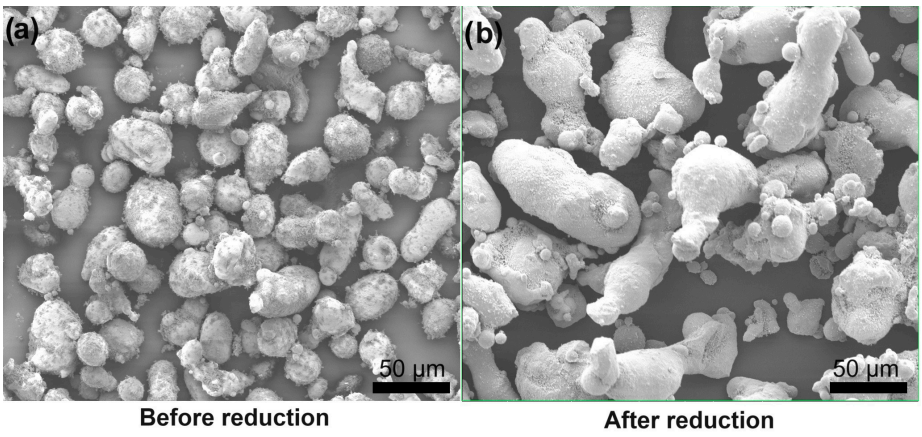


Figure 1. Morphology of the atomized powders: (**a**) before reduction and (**b**) after reduction.

3.2. Chemical Composition

Table 4 shows the elemental composition of the reduced powder and the alloys printed with four different conditions. It is evident that there was a notable reduction in the Mn content across all printed samples compared to the reduced powder. The reduced powder contained 17.59% Mn, while the printed samples exhibited a range of Mn content from 13.12% to 14.81%. The highest Mn content was observed in sample E3, with 14.81%, whereas sample E1 had the lowest Mn content at 13.18%. This decrease in Mn can be attributed to the demanganization phenomenon, which has been widely reported during the printing process due to the volatilization of Mn at high temperatures during energy input phases [30].

Table 4. Composition of the reduced powder and printed alloys.

Element	Mn (wt %)	C (wt %)	S (wt %)	Si (wt %)	Cr (wt %)	Mo (wt %)	O (wt %)	Fe (wt %)
Reduced powder	17.59	0.99	0.01	0.02	0.02	0.003	1.35	Bal.
E1	13.18	1.04	0.01	0.02	0.02	0.003	-	Bal.
E2	13.12	1.10	0.01	0.01	0.02	0.003	-	Bal.
E3	14.81	0.98	0.01	0.01	0.02	0.003	-	Bal.
E4	13.35	0.99	0.01	0.01	0.02	0.003	-	Bal.

Regarding carbon (C) content, there was a small variation among the printed samples. Sample E3 had the highest C content at 1.1026%, while the other samples showed values close to 1%. The reduced powder initially contained 0.9813% C, demonstrating a slight increase in carbon fraction after printing.

The presence of other elements such as Si, Cr, and Mo remained consistent across all samples, with no significant variation in composition, indicating these elements were stable during the printing process.

3.3. Structural Characterization of Printed Alloys

The X-ray diffraction (XRD) analysis was performed to identify the phase composition of the porous Fe-Mn-C alloy samples fabricated at different energy densities. The diffraction patterns, shown in Figure 2, reveal the presence of two primary phases: austenite ($CFe_{15.1}$) and manganese oxide (MnO).

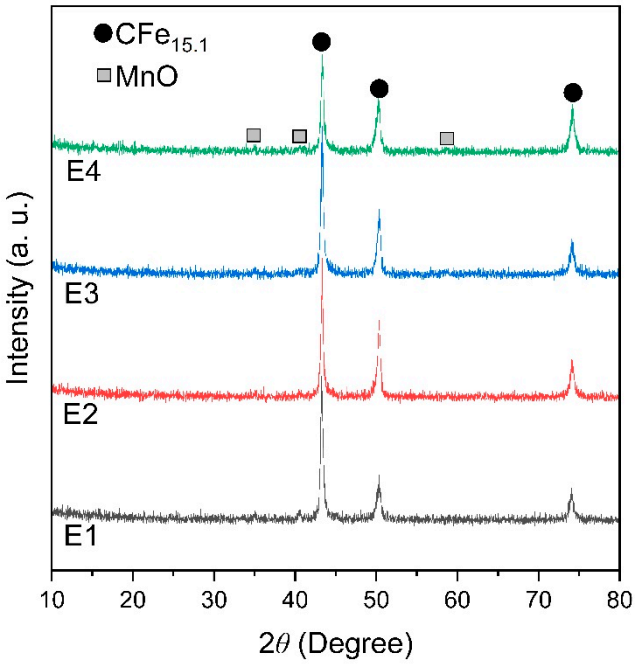


Figure 2. XRD patterns of the printed alloys.

For all energy densities, the predominant phase detected was austenite, with strong diffraction peaks located at 2θ values of approximately 43.5°, 50.7°, and 74.6°. The intensity of these peaks remains relatively consistent for all the conditions, indicating a stable presence of the austenitic phase regardless of the applied energy density. This suggests that the formation of austenite is not significantly influenced by variations in the energy input during the printing process.

In addition to austenite, MnO was observed in all the conditions, with characteristic peaks at 35.4° and 40.5°. The intensity of the MnO peaks appears to be similar in all printed samples, suggesting a similar fraction of MnO. MnO presence in the additively manufactured samples was attributed to the incomplete reduction and redistribution of this phase during the reduction and laser melting process.

Figure 3 shows SEM micrographs of the printed Fe-Mn-C alloy samples with two different magnifications. The low-magnification SEM micrographs (Figure 3a–d) show the evolution of porosity and pore morphology as a function of the energy density applied during the additive manufacturing process. In all samples, a network of interconnected pores is observed, indicative of the porous structure inherent to the selective laser melting (SLM) process. However, clear differences in pore size, distribution, and shape can be noted across the samples. The sample fabricated with the lowest energy density of 62.5 J/mm^3 (E1 sample) shows a highly irregular and interconnected porous structure, with larger pore sizes. The pores exhibit more irregular and jagged edges, the presence of many unmolten powder particles suggesting incomplete melting and consolidation of powder particles

at this lower energy input. As the energy density increases to 83.3 J/mm^3 (E2 sample), the porosity remains prominent, but the pore size appears to decrease slightly. The shape of the pores remains irregular, although the edges are somewhat smoother compared to the E1 sample, indicating better fusion between the powder particles. The E3 sample fabricated at 104.2 J/mm^3 shows a further reduction in pore size, with a more uniform distribution of smaller, rounded pores. The smoother edges of the pores suggest improved consolidation and melting at this energy level. The structure is more compact, indicating enhanced densification. At the highest energy density of 125.0 J/mm^3 (E4), the porosity is similar to that found in the E3 sample; however, the pores are shallower, suggesting higher densification.

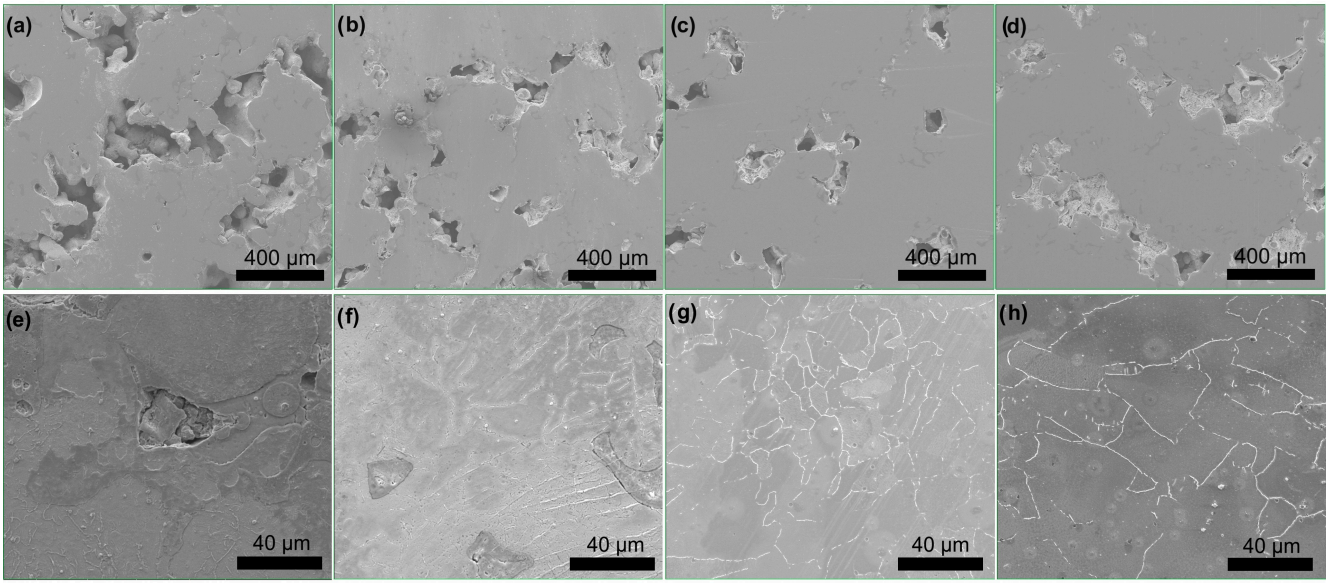


Figure 3. SEM micrographs of the printed Fe-Mn-C alloy samples at 2 different magnifications: E1: (**a**,**e**), E2: (**b**,**f**), E3: (**c**,**g**), E4: (**d**,**h**).

The high-magnification SEM micrographs (Figure 3e–h) allow for a closer examination of the microstructural features, including the morphology of the grain boundaries, potential cracks, and voids. The micrograph of the E1 sample (Figure 3e) shows evidence of larger, irregularly shaped grain boundaries, with some cracks and voids apparent within the structure. The presence of defects such as voids suggests incomplete melting or poor interparticle bonding at this lower energy density. In the E2 sample (Figure 3f), the grain boundaries are more defined, though they still exhibit some irregularity. The amount of cracks and voids was reduced compared to the E1 sample. The grains appear smoother, and the density is improved, but occasional defects are still present. The E3 and E4 samples exhibit more refined microstructure (Figure 3g,h), with well-defined, continuous grain boundaries and no cracks or voids. The grains appear smaller and more uniformly distributed, indicating a higher degree of melting and fusion. The sample E3 shows the smallest average grain size, measuring between 10 and 40 µm, while the E4 sample demonstrates the larger mean grain size, reaching approximately 100 µm.

Figure 4 shows energy-dispersive X-ray spectroscopy (EDS) elemental maps of Fe, Mn, C, and O for the printed Fe-Mn-C alloy samples. The EDS data reveal that iron (Fe) is the predominant element within the matrix of all samples, consistent with the expected composition of the alloys. Manganese (Mn) and oxygen (O) are predominantly accumulated around the pores, suggesting the presence of manganese oxide (MnO) at these locations, which is also supported by the XRD analysis. C is distributed more evenly and shows the lowest fraction in all the printed samples.

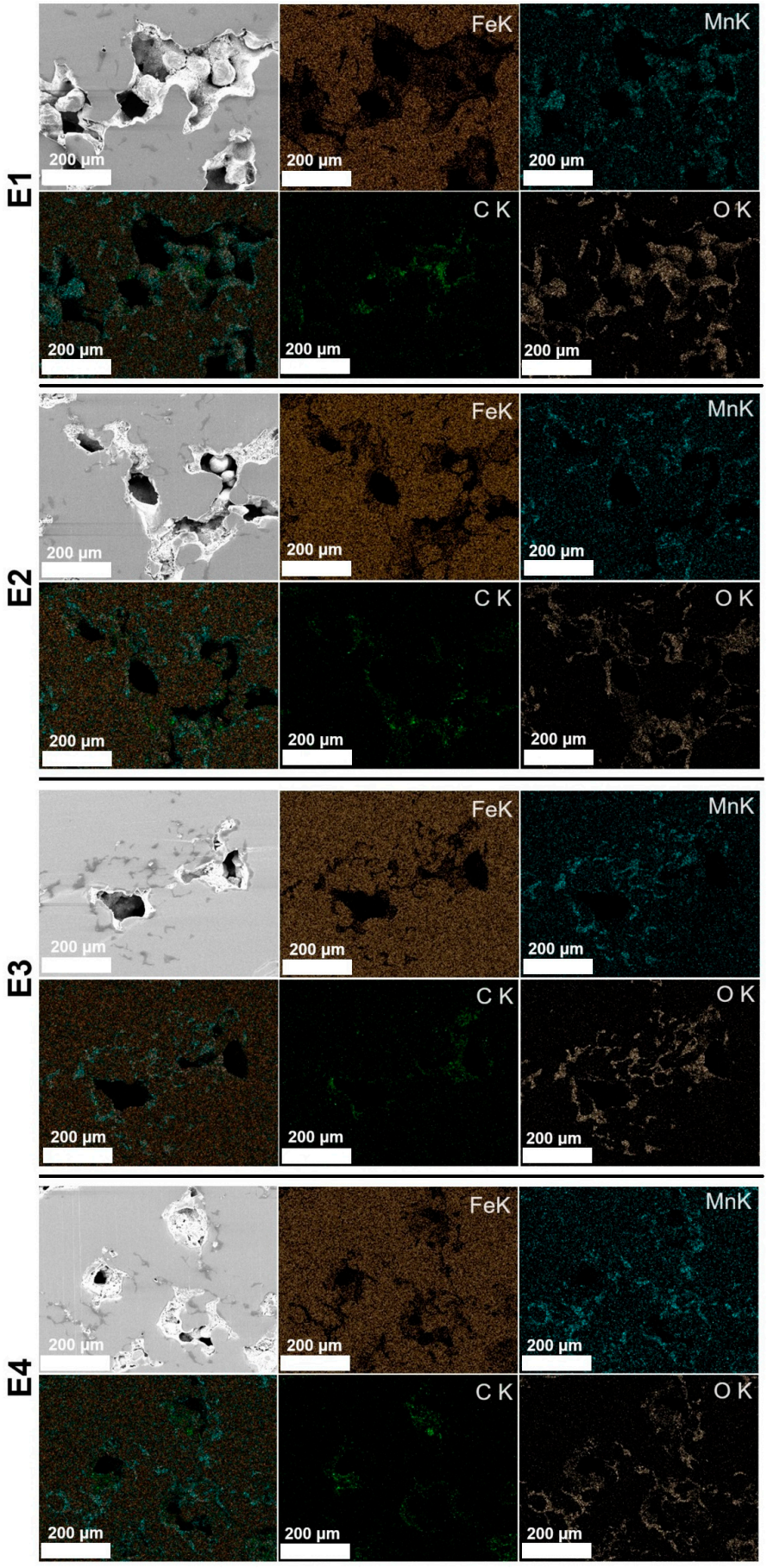


Figure 4. EDS mapping analysis on the surface of 4 printed alloys.

3.4. Degradation Behavior

Figure 5 presents the degradation rates of the four printed alloys immersed in modified Hanks' salt solution (MHSS) after 14 days of immersion. The sample E1 printed at the lowest energy density exhibits a relatively high degradation rate, approximately 1.34 mm/year. This elevated degradation rate is likely due to the high porosity and incomplete fusion observed in the microstructure, which can lead to increased surface area exposed to corrosive environments. When the energy density is increased to 83.33 J/mm^3 (E2 sample), the degradation rate decreases significantly to around 0.78 mm/year. The decrease in degradation rate is attributed to the fact that the microstructure at this energy level is more compact and better fused, resulting in fewer defects and reduced porosity. Interestingly, the degradation rate increases again and obtains the highest rate at approximately 1.62 mm/year for the E3 sample. While further densification of the material typically occurs at this energy density, with fewer pores and defects, the highest degradation rate of this sample is attributed to the smallest grain size and the highest amount of Mn in the sample. The E4 sample printed at the highest energy density (125.0 J/mm^3) shows the lowest degradation rate, approximately 0.17 mm/year. The significant decrease in degradation rate at this energy density is due to the highly dense microstructure with minimal porosity and defects and the larger grain sizes in these samples.

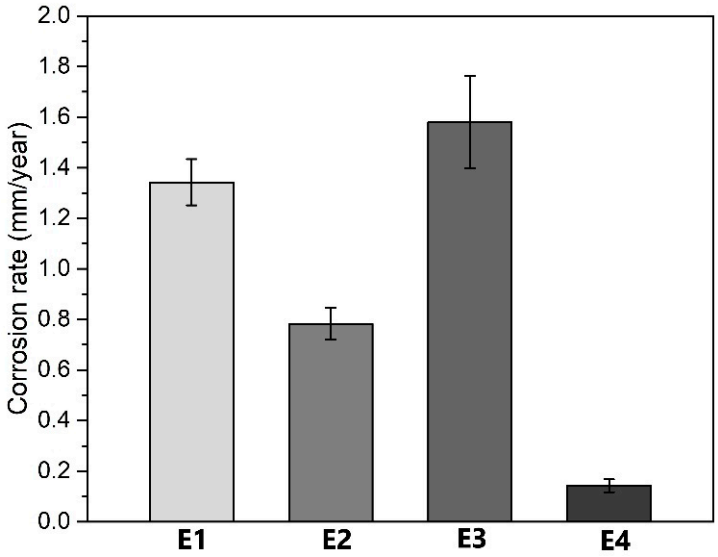


Figure 5. Degradation rate of the alloys after immersion test.

Figure 6 shows and compares the SEM micrographs of the alloy samples before (a–d) and after (e–h) immersion. As for E1 samples, significant corrosion of the porous structure is observed, with degradation products filling many of the pores. Corrosion has also caused considerable surface roughening on the E2 samples and filling of pores with degradation products. However, the degradation is less severe compared to the E1 sample. Sample E3 also displays a corroded surface, but only a small amount of degradation product adhered to and filled the pores. Inversely, the highest amount of degradation products attached to the surface of sample E4 following the interconnected pores.

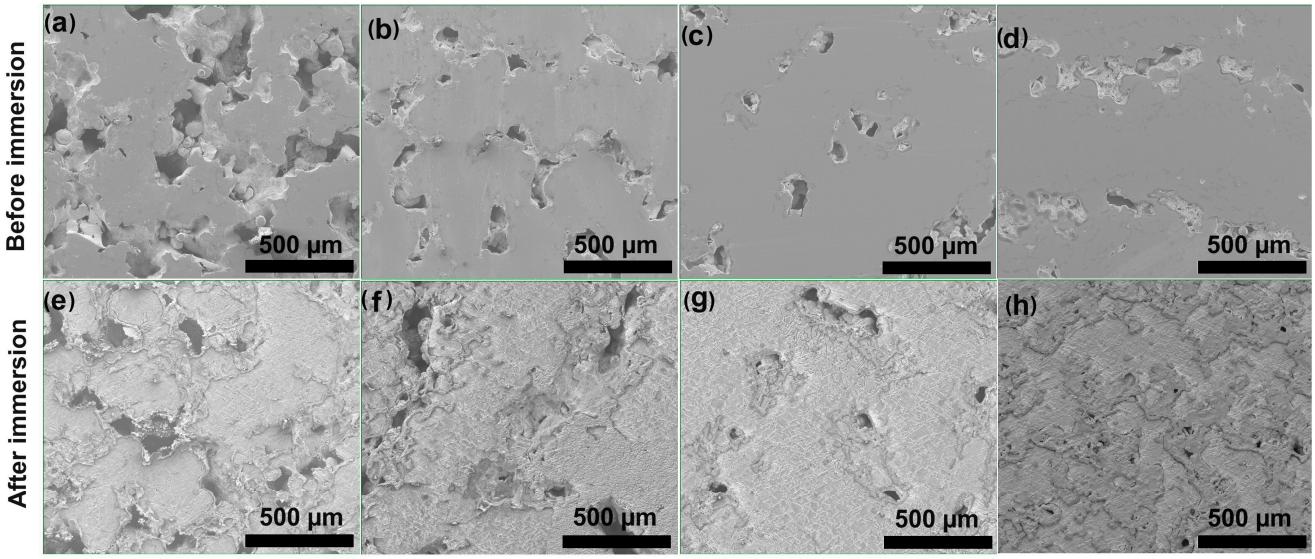


Figure 6. Morphology of the samples before and after the immersion test: E1: (**a**,**e**), E2: (**b**,**f**), E3: (**c**,**g**), E4: (**d**,**h**).

Figure 7 presents EDS elemental maps of the surface of the E4 sample after immersion; a similar result was obtained for three other samples. The result shows the distribution of Fe, Mn, C, O, Ca, and P on the surface of the sample. The analysis of these elemental maps suggests the formation of corrosion products, particularly focusing on the formation of manganese carbonate ($MnCO_3$) and calcium phosphate, both of which have been observed as degradation products in similar alloy systems [7,10]. The co-localization of manganese (Mn), carbon (C), and oxygen (O) around the pore strongly suggests the formation of manganese carbonate ($MnCO_3$). The presence of calcium (Ca), phosphorus (P), and oxygen (O) in certain regions indicates the formation of calcium phosphate compounds as a second degradation product with a lower amount.

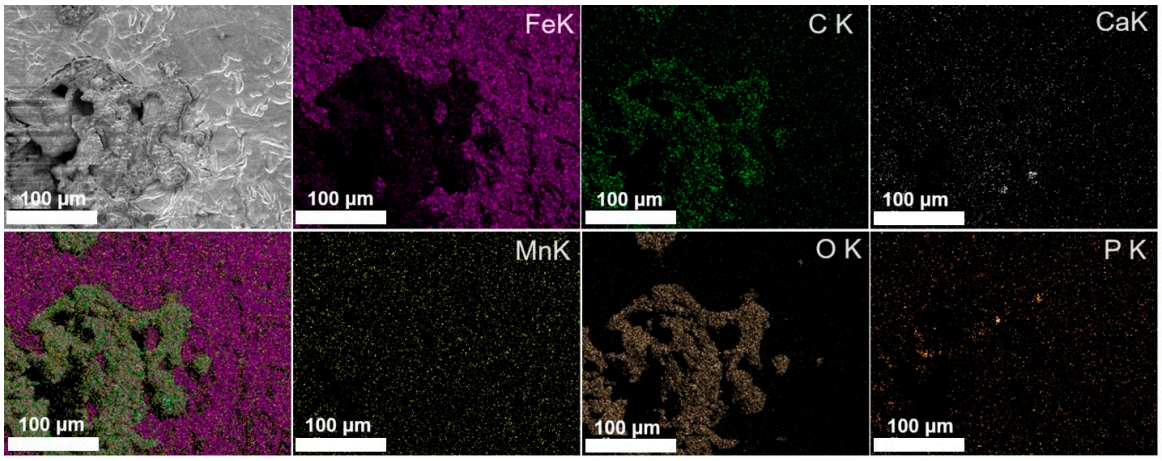


Figure 7. EDS mapping analysis on the surface of E4 sample after the immersion test.

Figure 8 presents SEM micrographs along with EDS analysis of the degradation products collected from the solution after the immersion test. For the E1 and E2 samples, the degradation products are characterized by irregularly shaped particles with sizes ranging from approximately 10 to 20 µm. These particles exhibit a rough, non-uniform morphology, indicating rapid formation and accumulation during the degradation process. In contrast, the degradation products collected from the solution containing E3 and E4 samples appear as much finer precipitate.

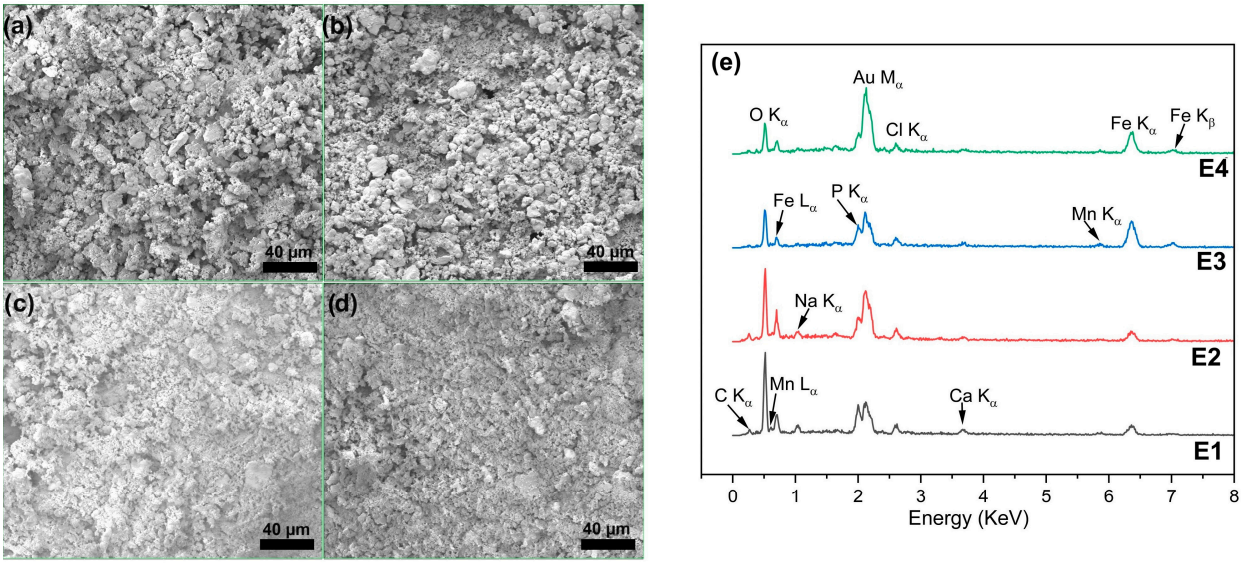


Figure 8. SEM micrographs and EDS analysis of the degradation products collected from the solution after the immersion test: (**a**) E1, (**b**) E2, (**c**) E3, (**d**) E4, (**e**) EDS analysis.

The EDS spectrum of the degradation products shows signals for carbon (C), manganese (Mn), oxygen (O), calcium (Ca), chlorine (Cl), and sodium (Na). The presence of O, C, and Mn peaks suggests that the degradation products are rich in Mn-containing compounds, likely manganese carbonates. The presence of calcium could be linked to the formation of calcium phosphate, which could have precipitated from the solution during the immersion test [7,10,12].

Figure 9 shows the FTIR spectra of degradation products collected after the immersion test. The spectra highlight the characteristic functional groups present in the degradation products, focusing on the identification of carbonate (CO_3^{2-}) and phosphate (PO_4^{3-}) groups. All samples show peaks corresponding to the presence of both CO_3^{2-} (carbonate) and PO_4^{3-} (phosphate) groups. The peak at around 1150–1250 cm^{-1} is attributed to the stretching vibrations of the carbonate ion (CO_3^{2-}), while the peak at approximately 1040–1100 cm^{-1} corresponds to the phosphate ion (PO_4^{3-}) stretching mode. These signals confirm the degradation products consist of $MnCO_3$ and calcium phosphates. The peaks corresponding to carbonate and phosphate in the degradation products of samples E1 and E3 exhibit higher intensity compared to those in samples E2 and E4.

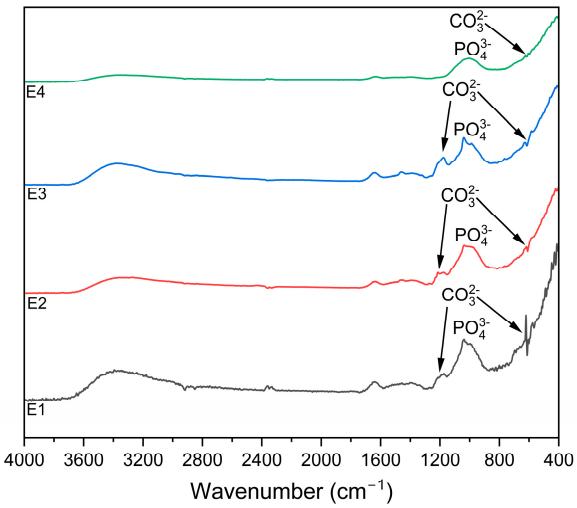


Figure 9. FTIR spectra of degradation products collected after the immersion test.

4. Discussion

4.1. Effect of Printing Energy on the Microstructure of the Alloys

It is evident from the analysis that printing energy has a strong impact on the microstructure of 3D-printed porous Fe-Mn-C alloys, which directly impacts their degradation behavior. At low printing energy levels, as observed in sample E1 (Figure 3a), inadequate energy results in insufficient melting of the unmelted powder particles, leading to the formation of large and deep pores. The observed correlation between low energy density and increased porosity aligns with previous research that highlights how insufficient energy input leads to poor particle bonding and enhanced void formation. For instance, studies by Yadroitsev et al. [31] and Sames et al. [32] demonstrate that low energy densities result in incomplete melting and significant porosity.

In contrast, increasing the printing energy density, as seen in samples E2 (Figure 3b) and E3 (Figure 3c), generally improves the microstructure. Higher energy levels facilitate more effective melting and bonding of the powder particles, resulting in a denser and more homogeneous microstructure. This is evidenced by the clearer grain boundaries and more highly crystallized structure in these samples (Figure 3f,g). Enhanced densification achieved through higher energy densities is known to improve mechanical properties. For example, Donik et al. [33] demonstrated that higher energy densities lead to reduced porosity and improved mechanical properties by promoting better particle fusion and minimization of internal voids.

However, excessively high energy densities introduce new challenges. For instance, the E4 sample shows the formation of interconnected pores, which can be attributed to phenomena such as evaporation and the Marangoni effect [34]. The Marangoni effect, driven by surface tension gradients in the molten pool, can cause instability and result in the entrapment of gas, leading to increased porosity and surface defects [35].

In addition to its effects on pore density and densification, printing energy density significantly impacts the grain size of the printed alloys. As illustrated in Figure 3e–h, increasing the energy density up to 104.2 J/mm^3 results in a noticeable reduction in grain size. This phenomenon can be attributed to the enhanced thermal conditions provided by higher energy inputs during the printing process. At elevated energy densities, the higher thermal input promotes more uniform melting and faster solidification of the powder particles [36,37]. This accelerated solidification leads to a finer grain structure due to the increased nucleation rate and reduced growth time for individual grains. Heidowitzsch et al. [38] demonstrated that higher energy densities in laser additive manufacturing led to finer grains due to more rapid cooling rates and reduced diffusion distances during solidification. This correlation is crucial, as finer grains often contribute to better overall performance in biomedical applications by improving mechanical properties and degradation rates [39].

A finer grain structure typically results in high-energy grain boundaries, which significantly influence corrosion susceptibility. [40]. Grain boundaries represent regions of atomic misalignment and higher energy compared to the interior of grains, making them more chemically reactive [41]. This elevated energy state results in preferential attack during corrosion, particularly in environments where localized electrochemical activity is significant [42]. The increased density of grain boundaries in alloys with smaller grains amplifies this effect, as a larger proportion of the material's surface area is susceptible to corrosion.

Microscopic stress distribution further compounds the susceptibility of small grains and high boundary density to corrosion. The rapid solidification associated with high energy densities often results in residual stresses within the microstructure, particularly near grain boundaries [36]. These stresses can arise due to the differential cooling rates

between adjacent grains or between the surface and interior regions of the alloy. Research by Takakuwa et al. [43] indicated that residual stresses can act as stress concentrators, exacerbating localized corrosion processes. In finer-grained materials, where grain boundaries are more prevalent, these stress concentrations are more uniformly distributed but remain critical sites for corrosion initiation.

Sample E3, with its smallest grain size and highest boundary density, exhibits the highest degradation rate among the samples studied. This behavior is consistent with the above mechanisms. The dense network of grain boundaries in E3 likely increases the overall reactivity of the material, while the residual stresses at these boundaries further amplify the degradation process.

However, it is essential to consider the limitations of increasing energy density. Excessively high energy densities lead to grain coarsening, as seen in Sample E4 printed with the energy density increased up to 125.0 J/mm^3 (Figure 3d,h). Larger grains reduce the density of grain boundaries, thereby lowering the material's overall susceptibility to grain boundary-driven corrosion. This trend aligns with findings by Kar et al. [44], who observed that coarser grains generally exhibit better corrosion resistance due to the reduced reactive area of grain boundaries.

4.2. Effect of Microstructure on the Degradation Behavior

The impact of printing energy on grain size, pore density, and densification is fundamental for understanding the degradation behavior of the printed alloys.

As printing energy increases, it generally enhances the densification of the printed alloys by promoting better melting and fusion of the powder particles [44]. This results in a denser microstructure with reduced pore density. Previous studies have demonstrated that higher pore density is associated with increased degradation rates. This is because a greater number of pores provides more surface area for the corrosive solution to interact with the alloy, leading to accelerated corrosion processes [45]. The presence of pores also increases the potential for localized corrosion, as the solution can penetrate deeper into the material, accelerating degradation. In this study, sample E1, despite having a significant amount of degradation product attached to the pore sites, exhibits a relatively high degradation rate. This can be attributed to its high pore density and low densification. The high pore density in E1 means that the corrosive solution has a larger contact area and deeper penetration, resulting in more extensive corrosion. Additionally, the low densification of this sample means that the powder particles did not fuse completely, leaving behind more internal voids that can exacerbate corrosion through mechanisms such as mechanical corrosion and stress concentration [46].

Sample E3 demonstrates the highest degradation rate among the samples studied, which can be attributed to several interrelated factors. Firstly, the microstructure of E3, characterized by its smallest grain size and highest density of grain boundaries, significantly contributes to its elevated degradation rate. The small grain size observed in sample E3 is associated with an increased number of grain boundaries. Research has consistently shown that smaller grain sizes can lead to higher degradation rates due to the increased surface area of grain boundaries, which are more susceptible to corrosion processes [39–43].

Grain boundaries serve as preferential sites for corrosion because they often possess higher energy states compared to the grain interiors, making them more reactive to corrosive environments [41,42]. Additionally, the high density of grain boundaries in E3 amplifies this effect, as a larger proportion of the material's surface area becomes susceptible to localized corrosion.

The role of manganese (Mn) segregation at grain boundaries further accelerates the corrosion reaction. Sample E3 contains the highest Mn content among the studied samples,

which likely results in enhanced Mn segregation at the grain boundaries. Mn segregation creates localized electrochemical gradients that promote galvanic corrosion. In this mechanism, the Mn-enriched grain boundaries act as anodic sites relative to the surrounding grain interiors, driving localized dissolution of the material at these boundaries [47]. The galvanic potential difference between the Mn-rich boundaries and the grain interiors accelerates the anodic reaction, leading to rapid degradation.

Local chemical reaction kinetics at the grain boundaries also play a critical role in influencing the degradation rate. The segregation of Mn at grain boundaries alters the electrochemical properties of these regions, potentially lowering the activation energy required for corrosion reactions to proceed [48]. Mn segregation can catalyze redox reactions at the boundary sites, leading to increased electron exchange rates and faster dissolution of the material. For instance, Mn oxides or other Mn-rich phases can enhance the cathodic reaction by facilitating the reduction in dissolved oxygen or water, thereby increasing the overall corrosion rate [47,48].

The large grain size in sample E4 plays a significant role in reducing the degradation rate. Larger grains result in fewer grain boundaries per unit volume compared to samples with smaller grains. Since grain boundaries are more susceptible to corrosion, a lower density of these boundaries in sample E4 reduces the overall reactivity of the material [41–43].

In addition, the high amount of degradation product attached to the pore sites of sample E4 contributes to its lower measured degradation rate. Degradation products can form protective layers on the surface of the material, mitigating further corrosive attacks [10,12]. This phenomenon is particularly evident in samples with significant amounts of attached corrosion products, as these layers can act as barriers to further corrosive penetration. The presence of interconnected pores in sample E4 (Figure 3d) might facilitate the accumulation of these products along the pore surfaces, enhancing the protective effect and reducing the effective corrosion rate.

Compared to Fe-Mn-C alloys fabricated using conventional methods, the 3D-printed alloys investigated in this study exhibit significantly higher degradation rates. Specifically, the degradation rates of the printed alloys range from 0.17 mm/year to 1.62 mm/year, whereas Fe-Mn-C cast alloys reported in prior studies demonstrated maximum degradation rates of only 0.155 mm/year [7], 0.13 mm/year [9], and 0.165 mm/year [12]. This remarkable difference highlights the unique impact of the 3D printing process on alloy behavior. The enhanced degradation rates of the printed alloys can be attributed primarily to the porous microstructure introduced by the additive manufacturing process. This porosity increases the surface area exposed to the corrosive environment and allows for deeper penetration of the corrosive medium, accelerating the degradation process [45]. This finding was also reported by Pucha et al. [49], who observed that the micropores in 3D-printed Fe create numerous intricate sites that promote autocatalytic corrosion. Additionally, the rapid solidification associated with 3D printing promotes microstructural features, such as fine grains and a high density of grain boundaries, which further contribute to the material's susceptibility to corrosion [39–43]. These findings highlight the distinct influence of 3D printing in tailoring the degradation properties of Fe-Mn-C alloys, offering potential advantages for applications where controlled degradation is desirable.

5. Conclusions

This study systematically investigated the influence of printing energy density on the microstructure and degradation behavior of 3D-printed porous Fe-Mn-C alloys. Key conclusions drawn from the results are as follows:

- Energy Density and Microstructure: Lower energy density (62.5 J/mm^3) produced alloys with a high pore density and a significant presence of unmelted powder particles, indicating incomplete melting. In contrast, the alloy printed at 104.2 J/mm^3 had the lowest pore density and the smallest grain size, reflecting optimized energy input for the printing process. At the highest energy density (125.0 J/mm^3), the alloy exhibited a coarser grain structure, which directly impacted its degradation behavior.
- Degradation Behavior: Alloys with higher pore density (E1) and smaller grain size (E3) degraded at faster rates due to increased surface area exposure to the corrosive environment. However, the accumulation of degradation products, particularly around the pores, also played a role in moderating the degradation rate. In contrast, the alloy printed at 125.0 J/mm^3 (E4), with a larger grain size, demonstrated the lowest degradation rate.
- Degradation Products: EDS and FTIR analysis revealed that manganese carbonate ($MnCO_3$) was the primary degradation product across all samples, while calcium phosphate was identified as a secondary product.
- Process Optimization for Biodegradable Material Applications: The results highlight the importance of controlling printing energy density to tailor the microstructure and, consequently, the degradation rate of porous Fe-Mn-C alloys. For applications requiring controlled biodegradability, such as biomedical implants, careful tuning of printing parameters is critical to achieve the desired degradation performance.

Altogether, the above findings suggest that the sample printed at 104.2 J/mm^3 shows the smallest grain size and the smallest average pore size, with the highest degradation rate. This energy was therefore found to be the most suitable for biodegradable implant application materials, compatible with water atomized powder used in this study.

In conclusion, this research provides a first understanding of how energy density during 3D printing affects the microstructural characteristics and degradation behavior of Fe-Mn-C alloys produced from water-atomized powder. This offers some guidelines for further development in the field of biodegradable materials with customized biodegradation properties. In future works, complementary quantitative analysis will be carried out, especially concerning volumetric pore distribution, structural mechanical properties, in vitro and in vivo behavior.

Author Contributions: Conceptualization, Q.N.C., C.P. and D.M.; methodology, Q.N.C., A.C., C.H.M.B. and S.G.; software, S.G., P.M. and C.B.; validation, C.P., S.G., C.B. and D.M.; formal analysis, Q.N.C., A.C. and P.M.; investigation, Q.N.C., A.C. and C.H.M.B.; resources, C.B., D.M. and P.M.; data curation, Q.N.C., A.C. and C.P.; writing—original draft preparation, Q.N.C.; writing—review and editing, C.P., S.G., C.H.M.B., C.B. and D.M.; visualization, Q.N.C.; supervision, D.M. and C.B.; project administration, Q.N.C. and C.P.; funding acquisition, D.M. All authors have read and agreed to the published version of the manuscript.

Funding: This research was partially supported by the Ministry of Economy and Innovation of Quebec Province (PRIMA, Quebec-South Korea) and the Natural Science and Engineering Research Council of Canada (Discovery and Alliance).

Data Availability Statement: The original contributions presented in this study are included in the article. Further inquiries can be directed to the corresponding author.

Acknowledgments: Our sincere thanks to Francesco Copes for technical assistance and to Pascale Chevallier for help and guidance.

Conflicts of Interest: The authors declare no conflict of interest.

References

1. DebRoy, T.; Mukherjee, T.; Wei, H.L.; Milewski, J.O.; Elmer, J.W.; Zhang, W.; De, A. Additive manufacturing of metallic components–process, structure, and properties. *Prog. Mater. Sci.* **2020**, *92*, 112–224. [CrossRef]
2. Gu, D.D.; Meiners, W.; Wissenbach, K.; Poprawe, R. Laser additive manufacturing of metallic components: Materials, processes and mechanisms. *Int. Mater. Rev.* **2012**, *57*, 133–164. [CrossRef]
3. Thompson, S.M.; Bian, L.; Shamsaei, N.; Yadollahi, A. An overview of direct laser deposition for additive manufacturing; Part I: Transport phenomena, modeling and diagnostics. *Addit. Manuf.* **2015**, *8*, 36–62. [CrossRef]
4. Gąsior, G.; Szczepański, J.; Radtke, A. Biodegradable Iron-Based Materials—What Was Done and What More Can Be Done? *Materials* **2021**, *14*, 3381. [CrossRef] [PubMed]
5. Gorejová, R.; Haverová, L.; Oriňaková, R.; Oriňak, A.; Oriňak, M. Recent Advancements in Fe-Based Biodegradable Materials for Bone Repair. *J. Mater. Sci.* **2019**, *54*, 1913–1947. [CrossRef]
6. Rabeeh, V.P.M.; Hanas, T. Progress in manufacturing and processing of degradable Fe-based implants: A review. *Prog. Biomater.* **2022**, *11*, 163–191. [CrossRef]
7. Gambaro, S.; Paternoster, C.; Occhionero, B.; Fiocchi, J.; Biffi, C.A.; Tuissi, A.; Mantovani, D. Mechanical and Degradation Behavior of Three Fe-Mn-C Alloys for Potential Biomedical Applications. *Mater. Today Commun.* **2021**, *27*, 102250. [CrossRef]
8. Koyama, M.; Yamashita, T.; Morooka, S.; Sawaguchi, T.; Yang, Z.; Hojo, T.; Kawasaki, T.; Harjo, S. Microstructure and Plasticity Evolution During Lüders Deformation in an Fe-5Mn-0.1C Medium-Mn Steel. *ISIJ Int.* **2022**, *62*, 2036–2042. [CrossRef]
9. Conti, M.C.; Aquilina, D.; Paternoster, C.; Vella, D.; Sinagra, E.; Mantovani, D.; Cassar, G.; Schembri Wismayer, P.; Buhagiar, J. Influence of Cold Rolling on In Vitro Cytotoxicity and Electrochemical Behaviour of an Fe-Mn-C Biodegradable Alloy in Physiological Solutions. *Heliyon* **2018**, *4*, e00926. [CrossRef] [PubMed]
10. Lee, S.H.; Kim, K.H.; Van, D.; Nam, S. Effect of C-Mn Ratio on the Maximum Hardness and Toughness in TMCP Steels with an Identical Carbon Equivalent. *J. Mater. Res. Technol.* **2020**, *9*, 8916–8928. [CrossRef]
11. Liu, B.; Zheng, Y.F. Effects of Alloying Elements (Mn, Co, Al, W, Sn, B, C, and S) on Biodegradability and In Vitro Biocompatibility of Pure Iron. *Acta Biomater.* **2011**, *7*, 1407–1420. [CrossRef]
12. Mouzou, E.; Paternoster, C.; Tolouei, R.; Purnama, A.; Chevallier, P.; Dubé, D.; Prima, F.; Mantovani, D. In Vitro Degradation Behavior of Fe–20Mn–1.2C Alloy in Three Different Pseudo-Physiological Solutions. *Mater. Sci. Eng. C* **2016**, *61*, 564–573. [CrossRef]
13. Zhang, Y.; Roux, C.; Rouchaud, A.; Meddahi-Pellé, A.; Gueguen, V.; Mangeney, C.; Sun, F.; Pavon-Djavid, G.; Luo, Y. Recent Advances in Fe-Based Bioresorbable Stents: Materials Design and Biosafety. *Bioact. Mater.* **2024**, *31*, 333–354. [CrossRef]
14. Syarif, J.; Pratesa, Y.; Prasetyo, Y.; Harjanto, S. Ball Milling Effect on Corrosion and Biocompatibility Behavior of FeMnC Alloys Produced by Powder Metallurgy in Simulated Body Fluids Environment. *Metals* **2021**, *11*, 1597. [CrossRef]
15. Kraus, T.; Moszner, F.; Fischerauer, S.; Fiedler, M.; Martinelli, E.; Eichler, J.; Witte, F.; Willbold, E.; Schinhammer, M.; Meischel, M.; et al. Biodegradable Fe-Based Alloys for Use in Osteosynthesis: Outcome of an In Vivo Study After 52 Weeks. *Acta Biomater.* **2014**, *10*, 3346–3353. [CrossRef] [PubMed]
16. Murr, L.E.; Gaytan, S.M.; Medina, F.; Lopez, M.I.; Martinez, E.; Hernandez, D.H.; Wicker, R.B. Next-Generation Biomedical Implants Using Additive Manufacturing of Complex, Cellular and Functional Mesh Arrays. *Philos. Trans. R. Soc. A Math. Phys. Eng. Sci.* **2010**, *368*, 1999–2032. [CrossRef] [PubMed]
17. Purnama, A.; Hermawan, H.; Couet, J.; Mantovani, D. Assessing the Biocompatibility of Degradable Metallic Materials: State-of-the-Art and Focus on the Potential of Genetic Regulation. *Biomed. Pharmacother.* **2010**, *6*, 1800–1807. [CrossRef] [PubMed]
18. Putra, N.E.; Borg, K.G.N.; Diaz-Payno, P.J.; Leeflang, M.A.; Klimopoulou, M.; Taheri, P.; Mol, J.M.C.; Fratila-Apachitei, L.E.; Huan, Z.; Chang, J.; et al. Additive Manufacturing of Bioactive and Biodegradable Porous Iron-Akermanite Composites for Bone Regeneration. *Acta Biomater.* **2022**, *148*, 355–373. [CrossRef]
19. Salama, M.; Vaz, M.F.; Colaço, R.; Santos, C.; Carmezim, M. Biodegradable Iron and Porous Iron: Mechanical Properties, Degradation Behaviour, Manufacturing Routes and Biomedical Applications. *J. Funct. Biomater.* **2022**, *13*, 72. [CrossRef] [PubMed]
20. Li, Y.; Jahr, H.; Zhou, J.; Zadpoor, A.A. Additively Manufactured Biodegradable Porous Metals. *Acta Biomater.* **2020**, *115*, 29–50. [CrossRef] [PubMed]
21. Sun, X.; Chen, S.; Wang, L.; Cui, T.; Liang, J.; Chen, J.; Wang, M. Effects of Energy Density on Microstructure Evolution and Electromagnetic Interference Shielding Efficiency of Laser Cladding Fe84Nb7B9 Alloy. *J. Alloys Compd.* **2023**, *961*, 171149. [CrossRef]
22. Xie, M.; Li, F.; Zhou, S.; Lu, L.; Peng, F.; Zhang, L.; Zhang, Y.; Lu, Y. Effect of Laser Energy Density on Microstructure and Properties Cu–Fe–P Immiscible Alloys Fabricated by Laser Selective Melting: Heterogeneous and High Strength and Magnetic. *J. Mater. Res. Technol.* **2023**, *26*, 2759–2769. [CrossRef]

23. Kluczyński, J.; Sarzyński, B.; Dražan, T.; Łuszczek, J.; Kosturek, R.; Szachogłuchowicz, I. Influence of Process Parameters on Selected Properties of Ti6Al4V Manufacturing via L-PBF Process. *Materials* **2024**, *17*, 4384. [CrossRef]
24. King, W.E.; Anderson, A.T.; Ferencz, R.M.; Hodge, N.E.; Kamath, C.; Khairallah, S.A. Laser Powder Bed Fusion Additive Manufacturing of Metals; Physics, Computational, and Materials Challenges. *Appl. Phys. Rev.* **2015**, *2*, 041304. [CrossRef]
25. Everton, S.K.; Hirsch, M.; Stravroulakis, P.; Leach, R.K.; Clare, A.T. Review of In-Situ Process Monitoring and In-Situ Metrology for Metal Additive Manufacturing. *Mater. Des.* **2016**, *95*, 431–445. [CrossRef]
26. Nandhakumar, R.; Venkatesan, K. A Process Parameters Review on Selective Laser Melting-Based Additive Manufacturing of Single and Multi-Material: Microstructure, Physical Properties, Tribological, and Surface Roughness. *Mater. Today Commun.* **2023**, *35*, 105538. [CrossRef]
27. Herzog, D.; Seyda, V.; Wycisk, E.; Emmelmann, C. Additive Manufacturing of Metals. *Acta Mater.* **2016**, *117*, 371–392. [CrossRef]
28. Buchbinder, D.; Meiners, W.; Wissenbach, K.; Poprawe, R. Selective Laser Melting of Aluminum Die-Cast Alloy—Correlations Between Process Parameters, Solidification Conditions, and Resulting Mechanical Properties. *J. Laser Appl.* **2015**, *27*, S29205. [CrossRef]
29. Nace, A. *ASTM G31-12a: Standard Guide for Laboratory Immersion Corrosion Testing of Metals*; ASTM International: West Conshohocken, PA, USA, 2012; Volume 100.
30. Nilsén, F.; Flores Ituarte, I.; Salmi, M.; Partanen, J.; Hannula, S.-P. Effect of Process Parameters on Non-Modulated Ni-Mn-Ga Alloy Manufactured Using Powder Bed Fusion. *Addit. Manuf.* **2019**, *28*, 464–474. [CrossRef]
31. Yadroitsev, I.; Krakhmalev, P.; Yadroitsava, I. Hierarchical Design Principles of Selective Laser Melting for High Quality Metallic Objects. *Addit. Manuf.* **2015**, *7*, 45–56. [CrossRef]
32. Sames, W.J.; List, F.A.; Pannala, S.; Dehoff, R.R.; Babu, S.S. The Metallurgy and Processing Science of Metal Additive Manufacturing. *Int. Mater. Rev.* **2016**, *61*, 315–360. [CrossRef]
33. Donik, Č.; Kraner, J.; Paulin, I.; Godec, M. Influence of the Energy Density for Selective Laser Melting on the Microstructure and Mechanical Properties of Stainless Steel. *Metals* **2020**, *10*, 919. [CrossRef]
34. Ma, C.; Zhang, R.; Li, Z.; Liu, W.; Chen, J.; Hu, Z.; Dong, Z.; Guo, Y. An Integrated Multiscale Model to Study the Marangoni Effect on Molten Pool and Microstructure Evolution. *Integr. Mater. Manuf. Innov.* **2023**, *12*, 502–513. [CrossRef]
35. Sinha, S.; Mukherjee, T. Mitigation of Gas Porosity in Additive Manufacturing Using Experimental Data Analysis and Mechanistic Modeling. *Materials* **2024**, *17*, 1569. [CrossRef]
36. Shanmuganathan, P.K.; Purushothaman, D.B.; Ponnusamy, M. Effect of High Laser Energy Density on Selective Laser Melted 316L Stainless Steel: Analysis on Metallurgical and Mechanical Properties and Comparison with Wrought 316L Stainless Steel. *3D Print. Addit. Manuf.* **2023**, *10*, 383–392. [CrossRef]
37. Carluccio, D.; Bermingham, M.; Kent, D.; Demir, A.G.; Previtali, B.; Dargusch, M.S. Comparative Study of Pure Iron Manufactured by Selective Laser Melting, Laser Metal Deposition, and Casting Processes. *Adv. Eng. Mater.* **2019**, *21*, 1900049. [CrossRef]
38. Heidowitzsch, M.; Gerdt, L.; Samuel, C.; Maetje, J.-F.; Kaspar, J.; Riede, M.; López, E.; Brueckner, F.; Leyens, C. Grain Size Manipulation by Wire Laser Direct Energy Deposition of 316L with Ultrasonic Assistance. *J. Laser Appl.* **2023**, *35*, 032017. [CrossRef]
39. Wang, P.; Ma, L.; Cheng, X.; Li, X.G. Influence of Grain Refinement on the Corrosion Behavior of Metallic Materials: A Review. *Int. J. Miner. Metall. Mater.* **2021**, *28*, 1112–1126. [CrossRef]
40. White, A.A.; Best, S.M. Properties and Characterisation of Bone Repair Materials. In *Bone Repair Biomaterials*; Planell, J.A., Best, S.M., Lacroix, D., Merolli, A., Eds.; Woodhead Publishing Series in Biomaterials; Woodhead Publishing: Cambridge, UK, 2009; pp. 121–153. [CrossRef]
41. Guiso, S.; Brijou-Mokrani, N.; de Lamare, J.; Di Caprio, D.; Gwinner, B.; Lorentz, V.; Miserque, F. Intergranular Corrosion in Evolving Media: Experiment and Modeling by Cellular Automata. *Corros. Sci.* **2022**, *205*, 110457. [CrossRef]
42. Takakuwa, O.; Soyama, H. Effect of Residual Stress on the Corrosion Behavior of Austenitic Stainless Steel. *Adv. Chem. Eng. Sci.* **2015**, *5*, 62–71. [CrossRef]
43. Kar, S.; Yilmaz, A.; Traka, K.; Sietsma, J.; Gonzalez-Garcia, Y. Role of Grain Size and Recrystallization Texture in the Corrosion Behavior of Pure Iron in Acidic Medium. *Metals* **2023**, *13*, 388. [CrossRef]
44. Wang, D.; Wu, S.; Fu, F.; Mai, S.; Yang, Y.; Liu, Y.; Song, C. Mechanisms and Characteristics of Spatter Generation in SLM Processing and Its Effect on the Properties. *Mater. Des.* **2017**, *117*, 121–130. [CrossRef]
45. Yang, D.; Kan, X.; Gao, P.; Liu, L.; Fang, X.; Zhang, X.; Wei, Q.; Shi, Y. Influence of Porosity on Mechanical and Corrosion Properties of SLM 316L Stainless Steel. *Appl. Phys. A* **2022**, *128*, 51. [CrossRef]
46. Wang, G.; Liu, Q.; Rao, H.; Liu, H.; Qiu, C. Influence of Porosity and Microstructure on Mechanical and Corrosion Properties of a Selectively Laser Melted Stainless Steel. *J. Alloys Compd.* **2020**, *831*, 154815. [CrossRef]
47. Dong, Q.; Jia, Y.; Ba, Z.; Tao, X.; Wang, Z.; Xue, F.; Bai, J. Exploring the Corrosion Behavior of Mn-Implanted Biomedical Mg. *J. Alloys Compd.* **2021**, *873*, 159739. [CrossRef]

48. Ma, H.; Zhao, Y.; Feng, Y.; Yu, Z.; Sun, J.; Song, H.; Lyu, Z.; Liu, T.; Hu, R.; Li, Y.; et al. Effect of Mn Content on Corrosion and Mechanical Behaviors of Fe-Based Medium Entropy Alloy. *J. Mater. Res. Technol.* **2024**, *30*, 5632–5651. [CrossRef]
49. Putra, N.E.; Leeflang, M.A.; Minneboo, M.; Taheri, P.; Fratila-Apachitei, L.E.; Mol, J.M.C.; Zhou, J.; Zadpoor, A.A. Extrusion-Based 3D Printed Biodegradable Porous Iron. *Acta Biomater.* **2021**, *121*, 741–756. [CrossRef]

Disclaimer/Publisher's Note: The statements, opinions and data contained in all publications are solely those of the individual author(s) and contributor(s) and not of MDPI and/or the editor(s). MDPI and/or the editor(s) disclaim responsibility for any injury to people or property resulting from any ideas, methods, instructions or products referred to in the content.